Final Technical Report

External Grant Award Number G15AP00116

Spatial and Temporal Variations in Structure and Seismicity Distribution in the Salton Trough, California

08/01/2015-07/31/2016

Guoqing Lin
Department of Marine Geosciences
Rosenstiel School of Marine and Atmospheric Science
University of Miami
4600 Rickenbacker Cswy, Miami, FL 33149

Phone: (305) 421-4150, Fax: (305) 421-4632
Email: glin@miami.edu

External Grant Award Number G15AP00116

Spatial and Temporal Variations in Structure and Seismicity Distribution in the Salton Trough, California

Guoqing Lin

ABSTRACT

The Salton Trough is located along the southernmost section of the San Andreas Fault and sits over several other major fault systems in southern California, including the Imperial Fault and the San Jacinto Fault Zone. In this one-year project, we study the spatial and temporal variations in the seismic velocity and attenuation structures and seismicity distribution in the Salton Trough using seismic data recorded by the Southern California Seismic Network and the ANZA seismic network. We developed a three-dimensional seismic attenuation model (represented by Q_p) based on calculated t* values for the Salton Trough and nearby region, which provides an important complement to the existing velocity models for interpreting structural heterogeneity and fluid saturation of rocks in the study area. In order to examine the response to large remote earthquakes, we calculate the seismicity rate change in the study area corresponding to the 1999 Hector Mine earthquake. Our results show that induced seismicity does not respond to remote triggering of large earthquakes as actively as tectonic earthquakes, implying that the anthropogenic activity might have changed the stress state inside the geothermal field. We are also examining the possibility of the reactivation of detachment faults beneath the Salton Trough and Imperial Valley using an available focal mechanism catalog. In addition, we are estimating high-resolution in situ V_p/V_s ratios within similar event clusters using waveform cross-correlation data, which show fine-scale variations that are not observed in the tomographic models. In the long term, our results will improve knowledge of seismic structure, fault and basin geometry and the processes of rifting, sedimentation, and magmatism and contribute to models of regional deformation, crustal structure and seismic hazard, which will be important for evaluating the potential for significant ground motion amplification in the Salton Trough region. It will also help to constrain the triggering mechanisms by understanding how effective fluid is coupled with the stress state.

REPORT

1. Three-Dimensional Seismic Attenuation Model

Seismic attenuation can provide important independent constraints on rock composition, fluid content, and temperature that are distinct from those provided by compressional (P)- and shear (S)-wave velocities. Tomography has been applied to determine the three-dimensional (3-D) seismic attenuation structure in a way similar to velocity inversion. The simul2000 tomographic program (*Thurber*, 1993; *Eberhart-Phillips*, 1990; *Thurber and Eberhart-Phillips*, 1999) is one of the most widely used algorithms for attenuation tomography. During the inversion, the high-frequency decay rate of direct-wave amplitude spectra are used to determine the whole path attenuation, quantified by the frequency-independent attenuation operator t^* values. The t^* values for each source-receiver pair are then inverted for the 3-D attenuation structure, indicated by the inverse of quality factor Q, by tracing the ray paths through a given velocity model.

In this project, we developed a frequency-independent three-dimensional (3-D) seismic attenuation model (indicated by Q_p^{-1}) for the crust of the Salton Trough and the adjacent regions in southeastern Southern California (Figure 1, *Lin*, 2014). We used the simul2000 algorithm to invert the t^* values measured from amplitude spectra (Figure 2) of 23,378 P-wave arrivals of 1,203 events through a recently developed 3-D velocity model (*Lin*, 2013). The Q_p model has a uniform horizontal grid spacing of 5 km and the vertical node intervals range between 2 and 5 km down to 27 km depth. In Figure 3, we show map views and cross-sections of the resulting Q_p model. In general, the Q_p values increase with depth and agree with the surface geology in the shallow depth layers. Low Q_p values are observed in the Imperial Valley, which are consistent with the sedimentary deposits and may also reflect the presence of pore fluid in the active fault zones, whereas greatly elevated Q_p values are shown in the surrounding crystalline ranges. The new Q_p model provides an important complement to the existing velocity models for interpreting structural heterogeneity and fluid saturation of rocks in the study area.

2. Remotely Triggered Seismicity

Seismic activity in geothermal fields is generally high and has been shown correlated with the production of geothermal energy (*Brodsky and Lajoie*, 2013; *Ellsworth*, 2013). The constantly high rate of seismicity may pose severe seismic hazard in the future (*Ellsworth*, 2013; *Deichmann and Giardini*, 2009). However, the complexity of stress perturbation makes it difficult to estimate whether the stress in these geothermal fields is close to the critical state. Our study in the Coso geothermal field, California, shows that induced seismicity does not respond to remote triggering of large earthquakes as actively as tectonic earthquakes, implying that the anthropogenic activity might have changed the stress state inside the geothermal field (*Zhang et al.*, 2016; *Lin and Zhang*, 2016). The Salton Sea region is geologically active and contains abundant geothermal resources. The largest development is located on the southeast shore of the Salton Sea, and is aptly called the Salton Sea geothermal field. The Salton Sea Geothermal Field (SSGF) was first developed in the early 1980s with a total potential resource of 2,000 megawatts electric. Similar to the Coso Geothermal Field, the Salton Sea Geothermal Field is also characterized by transtensional tectonic regime with highly active seismicity, strong subsidence, and long-term geothermal fluid loss (Fig-

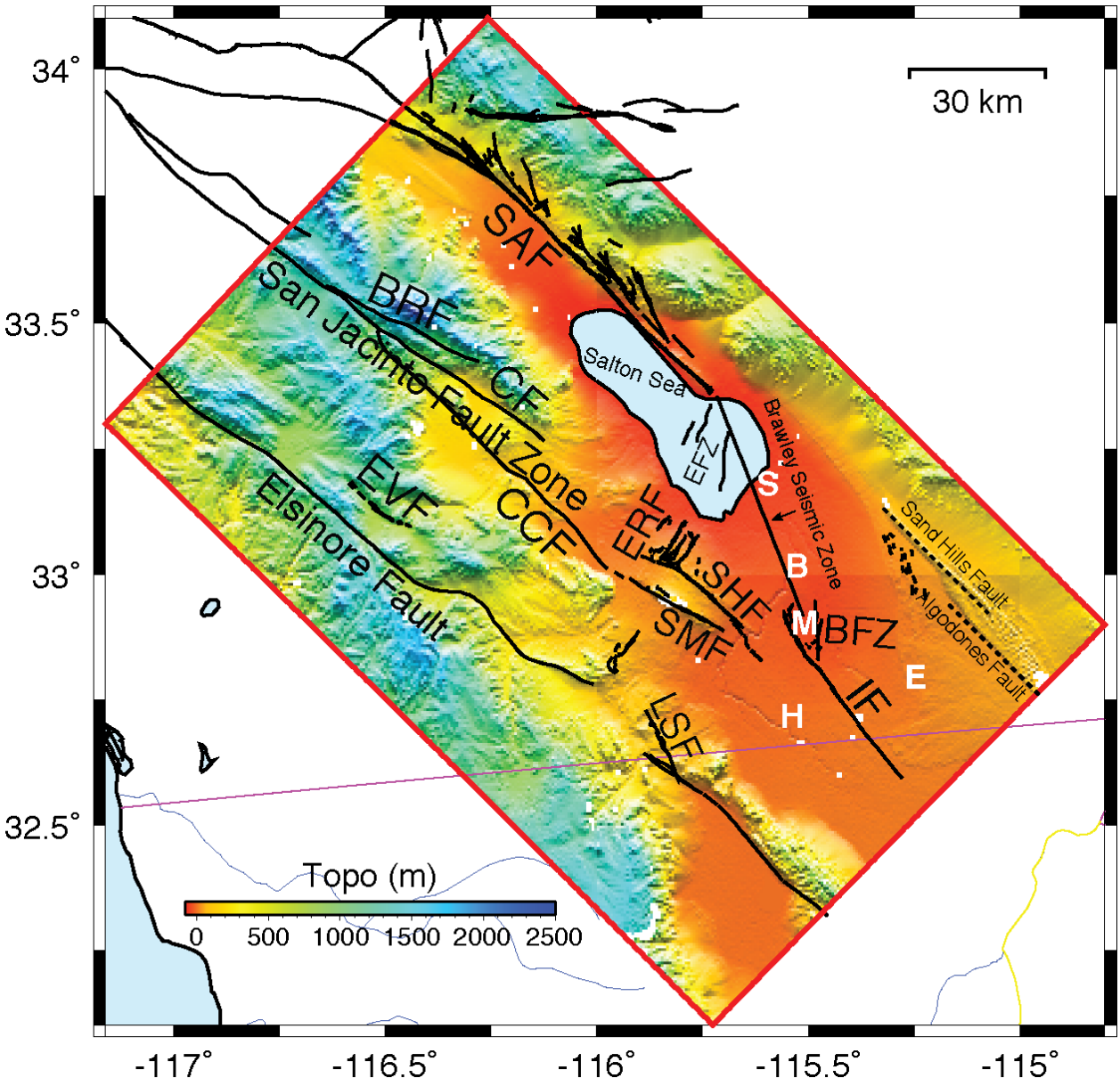

Figure 1. Major geological features in the study area, enclosed by the red box. Black lines denote major faults and the pink one the US-Mexico border. White letters show the locations of several major geothermal fields in this area, which are B, Brawley; E, East Mesa; H, Heber; M, Mesquite; and S, Salton Sea. Other abbreviations include BFZ, Brawley Fault Zone; BRF, Buck Ridge Fault; CCF, Coyote Creek Fault; CF, Clark Fault; EFZ, Extra Fault Zone; ERF, Elmore Ranch Fault; EVF, Earthquake Valley Fault; IF, Imperial Fault; LSF, Laguna Salada Fault; SAF, San Andreas Fault; SHF, Superstition Hills Fault; and SMF, Superstition Mountain Fault. The background is the topography base map (from U.S. Geological Survey). Figure is modified from *Lin* (2014).

ure 4) (*Brothers et al.*, 2009; *Brodsky and Lajoie*, 2013). In this project, we are using a relocated earthquake catalog (*Lin*, 2013) to examine the remote triggering in the Salton Sea area, which has been shown to respond to the 1999 Mw 7.1 Hector Mine earthquake (*Hough and Kanamori*, 2002;

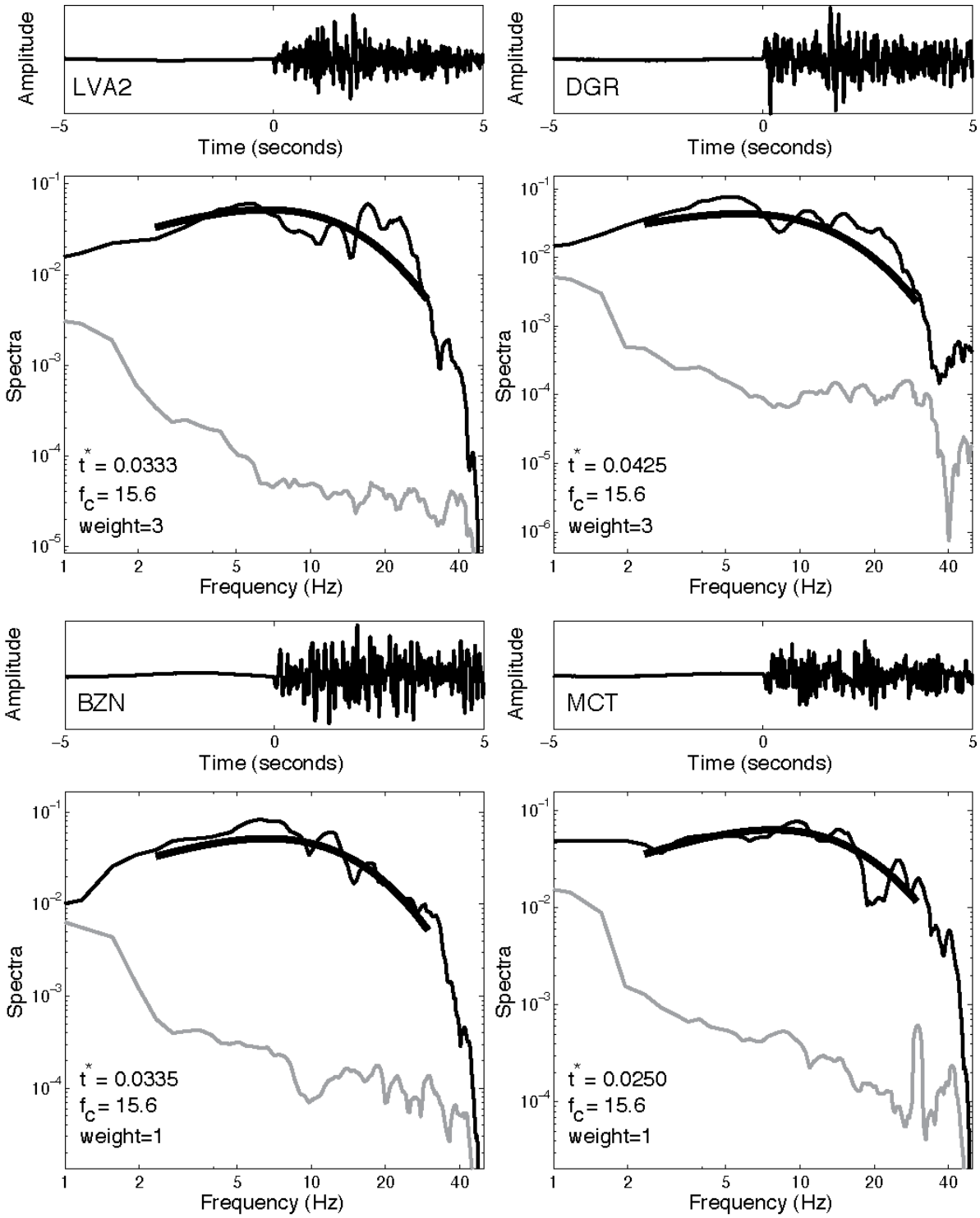

Figure 2. Examples of travel time series (top) and amplitude spectra (below) along with the computed t^* values, corner frequencies, and assigned weights for an event in the study area. Figure is modified from *Lin* (2014).

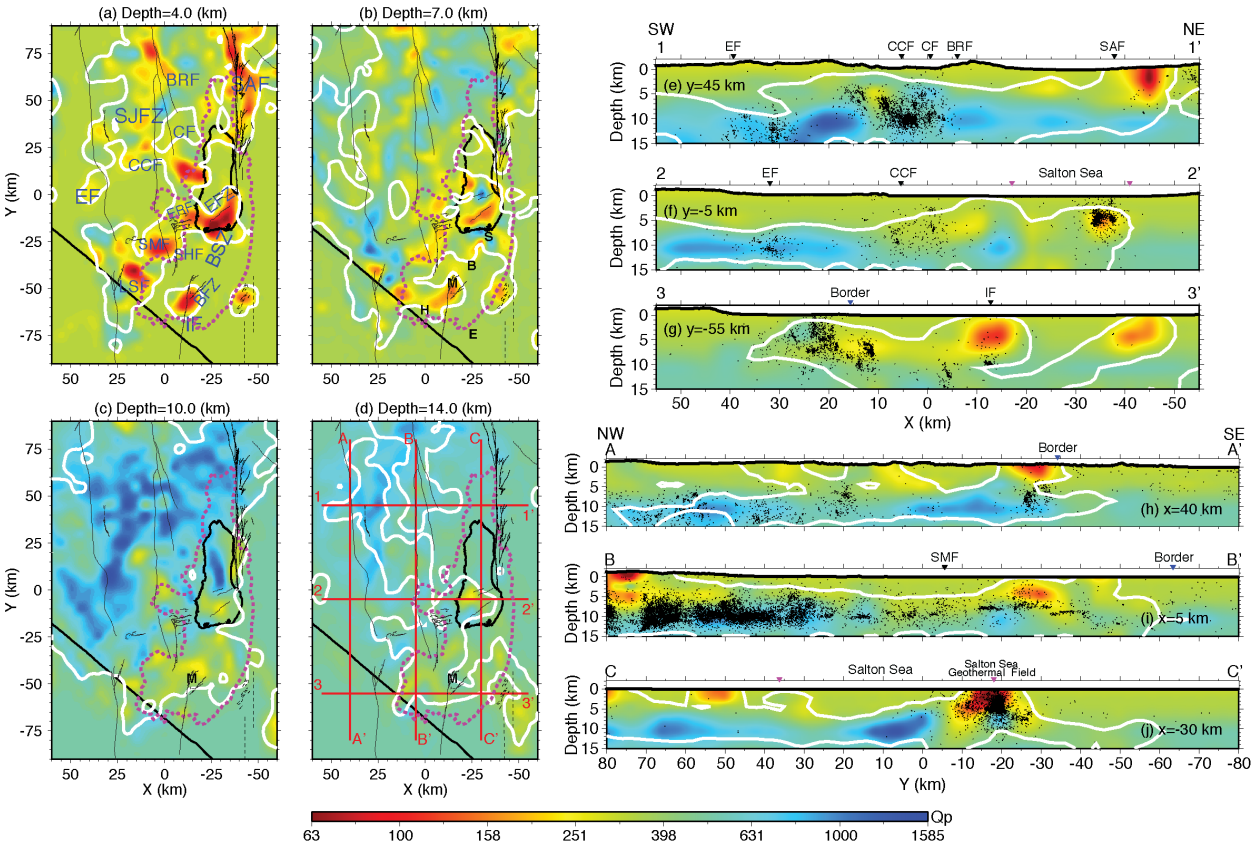

Figure 3. (a-d) Map views of the Q_p model at different depths. Black lines denote faults mapped at the surface, Salton Sea, and US-Mexico border; dotted pink one marks mean sea level. The white contours enclose the well-resolved area with the diagonal element of the resolution matrix greater than 0.1. Abbreviations in (a) are BFZ, Brawley Fault Zone; BRF, Buck Ridge Fault; BSZ, Brawley Seismic Zone; CCF, Coyote Creek Fault; CF, Clark Fault; EF, Elsinore Fault; EFZ, Extra Fault Zone; ERF, Elmore Ranch Fault; IF, Imperial Fault; LSF, Laguna Salada Fault; SAF, San Andreas Fault; SJFZ, San Jacinto Fault Zone; SHF, Superstition Hills Fault; and SMF, Superstition Mountain Fault. The geothermal areas in *Fuis et al.* (1982) are also marked in (b) as B, Brawley; E, East Mesa; H, Heber; M, Mesquite; and S, Salton Sea. The red straight lines in (d) are the profiles for the cross sections. (e-g) Cross sections through the Q_p model along the SW-NE profiles, including the relocated seismicity (black dots) from *Lin* (2013) within $\pm$3 km distance of the profile line. The white contours enclose the regions with the resolution above 0.1. Zero depth corresponds to mean sea level. The black curve at top of each cross section shows the local topography and small triangles mark the surface traces of the faults (black), the Salton Sea boundary (pink) and the US-Mexico border (blue). Abbreviations are EF, Elsinore Fault; SJFZ, San Jacinto Fault Zone; SAF, San Andreas Fault; CCF, Coyote Creek Fault; CF, Clark Fault; BRF, Buck Ridge Fault; Border, US-Mexico Border; SMF, Superstition Mountain Fault; SHF, Superstition Hills Fault; and IF, Imperial Fault. (h-j) Cross sections through the Q_p model along the NW-SE profiles. Figure is modified from *Lin* (2014).

Gomberg et al., 2001).

We calculate the seismicity rate change for 4 and 30 days after the Hector Mine earthquake relative to the background seismicity from 1996 to 2002 using the β-statistic (*Matthews and Reasenberg*,

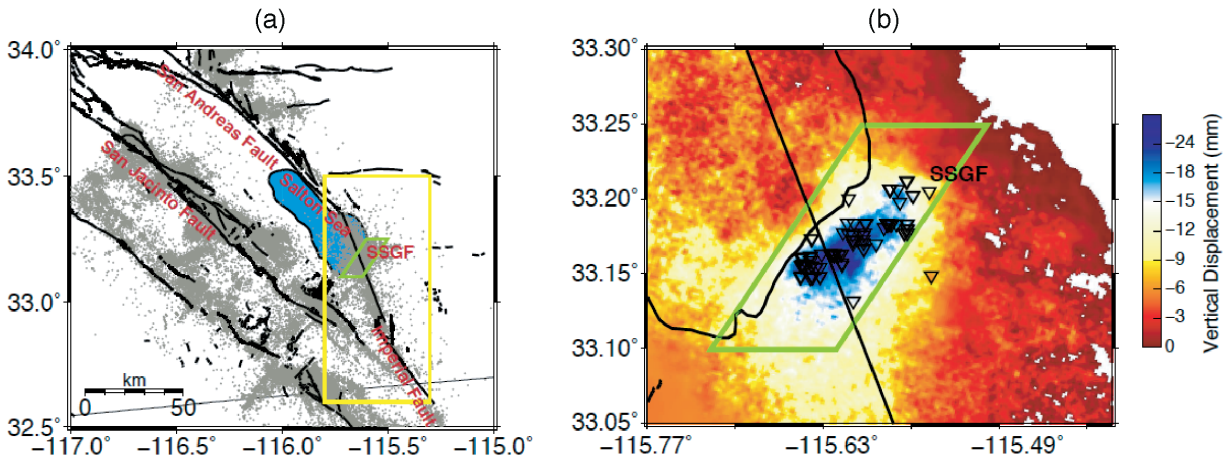

Figure 4. Tectonics and location of the Salton Sea geothermal field (SSGF). Green polygons outline the same location of the SSGF. (a) Tectonic map showing the faults and the background seismicity between 1981 and 2010. Yellow box encloses our entire study area, including the SSGF and its vicinity. The Salton Sea is shown in blue. (b) Locations of injection and extraction wells (black triangles), obtained from the California Oil, Gas, and Geothermal Resources (DOGGR). Background is accumulated subsidence in the SSGF that occurred between 2003 and 2010 from InSAR result (Heresh Fattahi, personal communication, 2014).

1988; *Reasenberg and Simpson*, 1992; *Kilb et al.*, 2000; *Hill and Prejean*, 2007), which compares the difference between the observed and expected seismicity in the selected time window, normalized by standard deviation of the expected seismicity. According to *Matthews and Reasenberg* (1988) and *Hill and Prejean* (2007), it can be expressed as the following

$$\beta(n_a, n_b, t_a, t_b) = \frac{n_a - E(n_a, n_b)}{\sqrt{\mathrm{var}(n_a, n_b)}} \tag{1}$$

where n_a and n_b are the numbers of earthquakes in the time period of t_a and t_b, respectively. $E(n_a,n_b)$ is the expected number of earthquakes in t_a based on the sample of background seismicity rate in t_b. $var(n_a, n_b)$ denotes the variance of the number of earthquakes in t_a based on the sample of the background seismicity rate in t_b. The study area is gridded with blocks of 5×6 km^2, which are chosen to ensure relatively uniform seismicity in different blocks. In Figures 5a and b, we show comparisons of the seismicity rate changes in different time windows (4 and 30 days) relative to the background seismicity. We observe increased seismicity within 5 km north and south of the SSGF, indicated by large β-values ($\sim$6) within 4 days after the Hector Mine earthquake. However, the seismicity inside the SSGF did not show an abrupt increase. The remotely triggered earthquake sequence identified by a previous study (*Hough and Kanamori*, 2002) also falls outside the geothermal field.

In order to compare the spatiotemporal variation of the seismicity at consistent spatial scales, we assign the geothermal field as subarea 1 and some adjacent areas into 3 subareas, including the Brawley Seismic Zone (BSZ) and Imperial Fault (IF) (black boxes in Figure 5a) based on the distribution of the background seismicity from 1996 to 2002. Figure 5c shows the time series

for all the 4 subareas in 1999. We observe an abrupt increase in the seismicity rates after the Hector Mine earthquake for all the 3 subareas outside the SSGF. In contrast, the geothermal field itself appears unaffected by the Hector Mine earthquake, which is consistent with our β-statistic analysis above. Therefore, the observed absence of remote triggering within the Coso Geothermal Field does not appear to be a special case. Our results will help understand how effective fluid is coupled with the stress state.

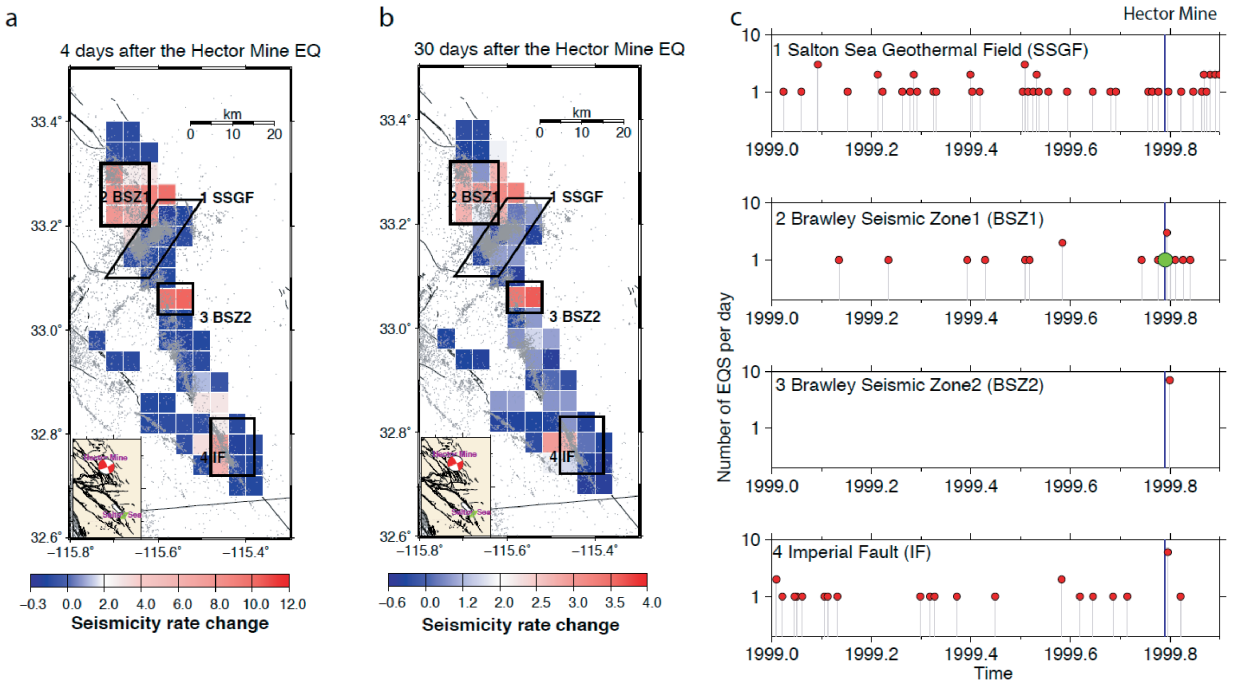

Figure 5. Seismicity rate change in the Salton Sea geothermal field (SSGF) and its vicinity. Map view of β-statistic of 4 days (a) and 30 days (b) after the 1999 Mw 7.1 Hector Mine earthquake relative to the background seismicity (1996-2002). Polygon outlines the SSGF based on the location of the active injection and extraction wells. Boxes mark the subareas outside of the geothermal field, including the Brawley Seismic Zone (BSZ) and Imperial Fault (IF). Grey dots denote the background seismicity from 1981 to 2010. Inset shows the location of the Hector Mine earthquake and the SSGF. (c) One-year time series in the SSGF and its vicinity. The first panel is the SSGF. The other three are the subareas outside the SSGF. Red dots represent microearthquakes with $1.7 \leq \text{Mw} < 4.0$ in the declustered catalog and green dots for $\text{Mw} \geq 4.0$. Blue line marks the onset of the Hector Mine earthquake.

3. Focal Mechanism Variations

One observation from the recent relocation catalog for our study area by *Lin* (2013) is the gently undulating surface seen at the base of seismicity in the Salton Trough, from the US-Mexico border to the north end of the Salton Sea (1-1' in Figures 6a and b). This observation may indicate the existence of detachment faults beneath the Salton Trough and Imperial Valley, which are associated with extensional tectonics. In order to test this hypothesis, we take advantage of the latest focal mechanism catalog for southern California by *Yang et al.* (2012). We compute the scalar faulting

type from the rakes of the two nodal planes, varying from -1 (normal) to 0 (strike-slip) to 1 (reverse) in order to characterize the focal mechanism of each event. This approach has the advantage of providing a single scalar value for characterizing the faulting type and has been used in previous studies (*Shearer et al.*, 2006; *Lin and Shearer*, 2009; *Lin and Okubo*, 2016). Figure 6 shows the map views and cross-sections of the scalar focal mechanisms in two time periods, 1981-2000 and 2001-2010.

These results show that events in the Brawley Seismic Zone are significantly dominated by strike-slip faulting. However, a 25% increase of normal faulting relative to previous years is observed in the Imperial Fault region starting in 2001, which may be associated with the existence or reactivation of a detachment fault. The fraction of normal faulting during the time period of 2001-2010 is comparable with the nearby Laguna Salada Fault Zone in the southwest portion of the study area, the seismicity over where is dominated by the aftershocks of the 2010 Baja California earthquake, which broke a detachment fault in the southeast of the study area. We are now investigating the cause of this focal type variation in the study area.

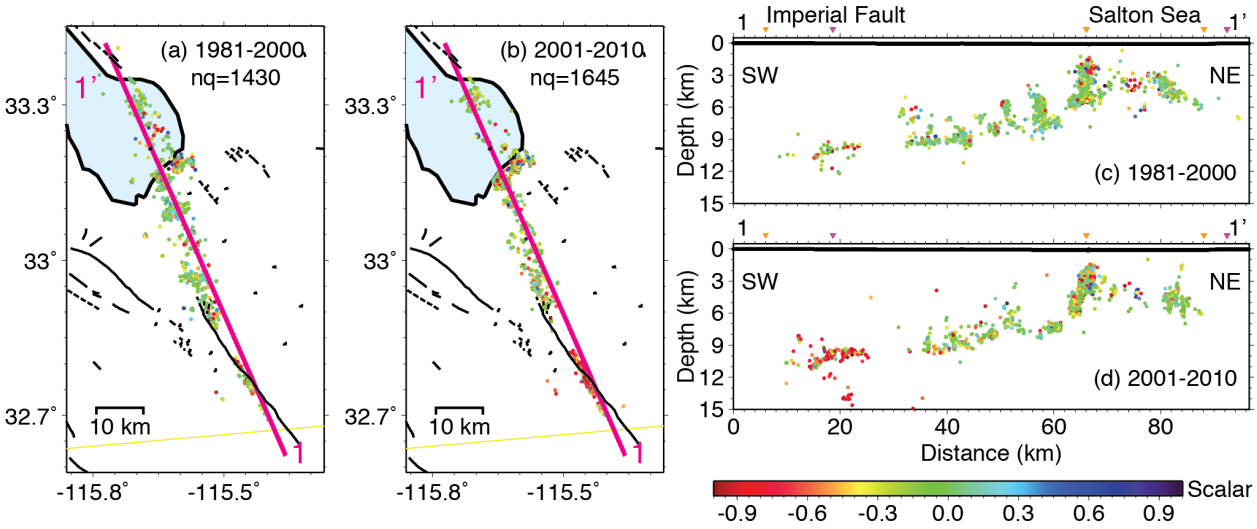

Figure 6. Quality A, B and C focal mechanisms in the Brawley Seismic Zone. Earthquakes are colored by their scalar solutions. Pink straight line in (a) and (b) is the profile for the cross-sectional views in (c) and (d). Dotted curves at top illustrate the local topography.

4. Estimation of In-Situ V_p/V_s Ratios

V_p/V_s ratio is directly related with Poisson's ratio and is more important than V_p and V_s separately in characterizing rock composition and crack and fluid properties. In order to complement the tomographic results (both velocity and attenuation), differential times resulting from waveform cross-correlation are being used to estimate high-resolution near-source V_p/V_s ratios within similar event clusters. We are applying the method developed by *Lin and Shearer* (2007) to estimate high-resolution near-source V_p/V_s ratios. It is shown that when both P- and S-wave differential times from waveform cross-correlation are available, it is possible to estimate the near-source V_p/V_s ratio with high precision because of the great accuracy of the waveform cross-correlation data. Equation

2 shows the basic idea of this method for a single pair of events in a similar event cluster recorded by a common station i.

$$(\delta t_s^i - \bar{\delta t_s}) = (\frac{V_p}{V_s})(\delta t_p^i - \bar{\delta t_p}) \tag{2}$$

where δt_p^i and δt_s^i are the differential P and S times, and $\bar{\delta t_p}$ and $\bar{\delta t_s}$ are the mean values of the differential times from all the stations. In this way we can estimate the local V_p/V_s ratio using the demeaned differential times from all event pairs in the cluster.

We apply the in situ V_p/V_s estimate approach to the 1,174 similar event clusters consisting of $\sim$100,000 earthquakes in our study area from *Lin* (2013) (Figure 7a). Standard uncertainties in the in situ V_p/V_s ratios are computed using a bootstrap approach (e.g., *Efron and Gong*, 1983; *Efron and Tibshirani*, 1991), in which the pairs of differential P and S times in the same cluster are randomly resampled 1000 times. As suggested by *Lin and Shearer* (2007), the most accurate V_p/V_s results for real data clusters are obtained for clusters with three-dimensional distributions of events. In order to estimate the spatial distribution of events in each cluster, we used the method of principal component analysis (e.g., *Kirschvink*, 1980) to compute eigenvalues for the covariance matrix of the earthquake locations for all similar event clusters. Clusters are considered to have nearly spherical distribution if $\lambda_1/\lambda_3 \leq K$, (where eigenvalues $\lambda_1 \geq \lambda_2 \geq \lambda_3$, K is a constant).

In this study, we select the clusters with $\lambda_1/\lambda_3 \leq 10$ and the estimated standard errors in V_p/V_s less than 0.03 as criteria for further in situ V_p/V_s analyses. The resulting 376 clusters consist of 86,253 well-relocated events (Figure 7b) and over 10 million differential times. The average interevent distance ranges from 0.9 to 4.5 km for all the clusters. The estimated in situ V_p/V_s ratios vary from 1.50 to 2.16. In Figure 8, we compare the in situ V_p/V_s ratios for events in similar event clusters with the 3-D seismic tomographic result. In Figure 8a, we project all the events in the study area along A-A'. In general, the in situ V_p/V_s ratios agree with the tomographic result (Figure 8c) with the average of 1.718. However, small scale V_p/V_s variations are observed. The comparison between the two V_p/V_s results along the Brawley Seismic Zone (Figure 8b and d) shows significantly low in situ values with an average of 1.606. A manuscript is being prepared on the in situ V_p/V_s results for the study area (*Lin*, 2016).

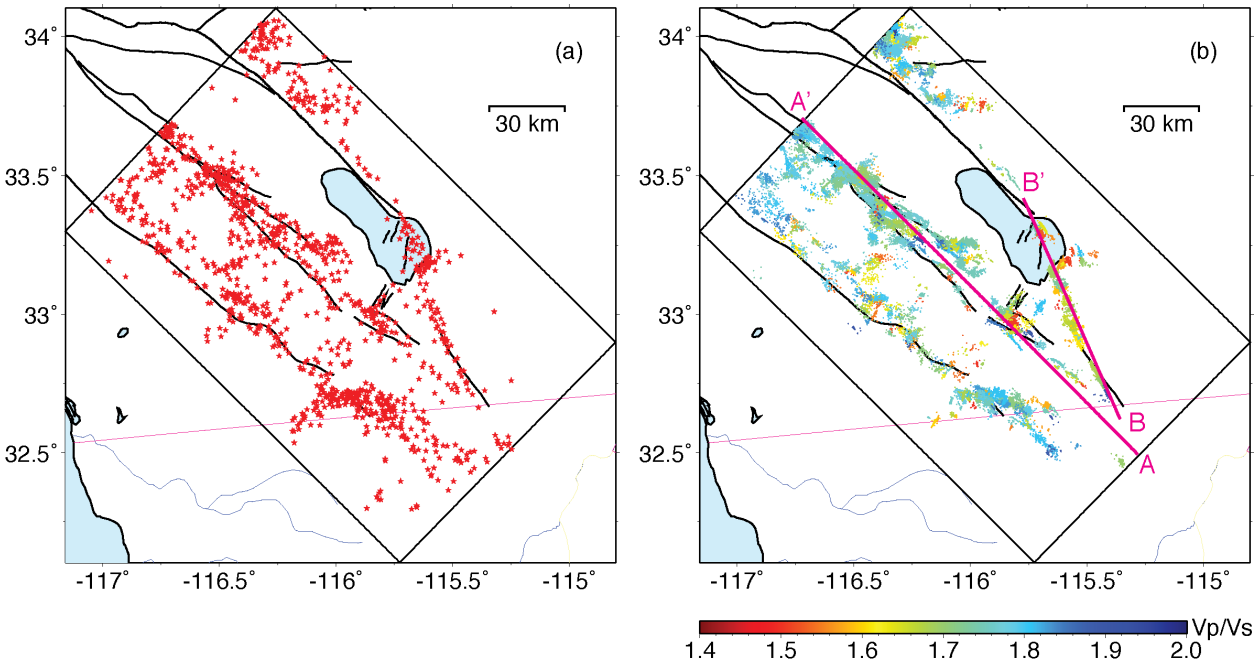

Figure 7. (a) Map of centroids of the 1,174 similar event clusters for the in situ V_p/V_s estimation. (b) Seismicity in the similar event clusters with robust in situ V_p/V_s ratios, colored by the estimated V_p/V_s value for each cluster. Note that events in the same cluster have the same V_p/V_s ratio, therefore the same color. The two pink straight lines are the profiles for the cross-sectional views in Figure 8.

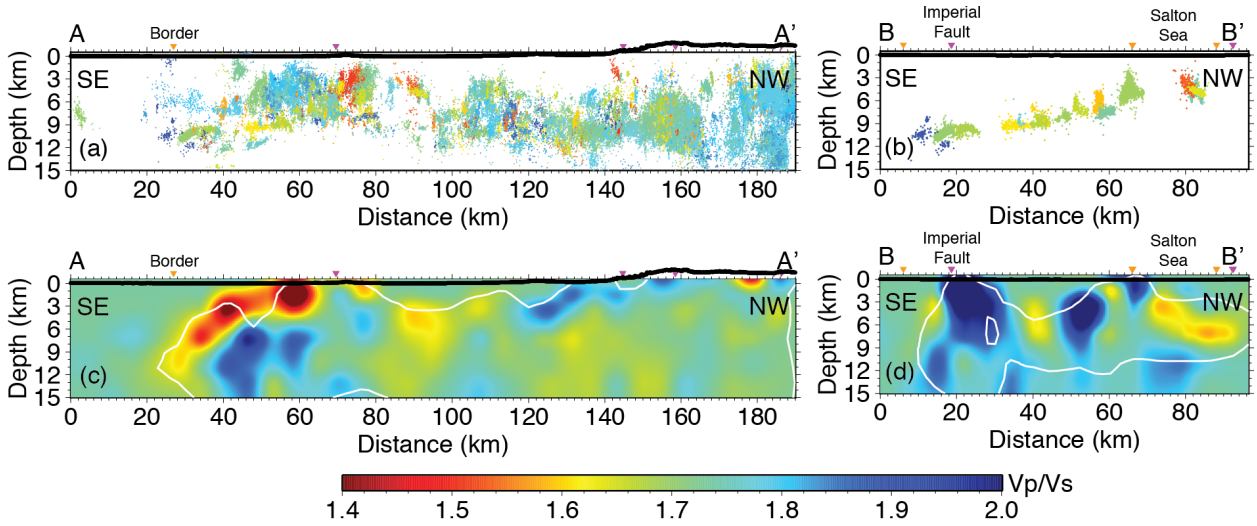

Figure 8. (a, b) Depth distributions of seismicity in the similar event clusters with robust in situ V_p/V_s values along the two profiles shown in Figure 7b. Note that all the events shown in Figure 7b are projected along A-A' in (a) and earthquakes within ± 3 km distance of the profile B-B' are shown in (b). (c, d) Cross sections through the tomographic V_p/V_s model by *Lin* (2013) along the same profiles. The white contours enclose the regions with the resolution above 0.5.

Bibliography *(∗ indicating references supported in full or part by this award)*

Brodsky, E. E., and L. J. Lajoie, Anthropogenic Seismicity Rates and Operational Parameters at the Salton Sea Geothermal Field, *Science*, *341*, 543–546, 2013.

Brothers, D. S., N. W. Driscoll, G. M. Kent, A. J. Harding, J. M. Babcock, and R. L. Baskin, Tectonic evolution of the Salton Sea inferred from seismic reflection data, *Nature Geosci.*, *2*, 581–584, 2009.

Deichmann, N., and D. Giardini, Earthquakes Induced by the Stimulation of an Enhanced Geothermal System below Basel (Switzerland), *Seismol. Res. Lett.*, *80*, 784–798, 2009.

Eberhart-Phillips, D., Three-dimensional P and S velocity structure in the Coalinga region, California, *J. Geophys. Res.*, *95*, 15,343–15,363, 1990.

Efron, B., and G. Gong, A leisurely look at the bootstrap, the jackknife and cross-validation, *Am. Statist.*, *37*, 36–48, 1983.

Efron, B., and R. Tibshirani, Statistical data analysis in the computer age, *Science*, *253*, 390–395, 1991.

Ellsworth, W. L., Injection-Induced Earthquakes, *Science*, *341*, 142–+, 2013.

Fuis, G. S., W. D. Mooney, J. H. Healey, G. A. McMechan, and W. J. Lutter, Crustal structure of the Imperial Valley region, *The Imperial Valley, California, Earthquake of October 15, 1979, U.S. Geol. Surv. Profess. Paper*, *1254*, 25–50, 1982.

Gomberg, J., P. Reasenberg, P. Bodin, and R. Harris, Earthquake triggering by seismic waves following the Landers and Hector Mine earthquakes, *Nature*, *411*, 462–466, 2001.

Hill, D. P., and S. Prejean, Dynamic triggering, *Treatise on Geophysics*, *4*, 257–291, 2007.

Hough, S. E., and H. Kanamori, Source Properties of Earthquakes near the Salton Sea Triggered by the 16 October 1999 M 7.1 Hector Mine, California, Earthquake, *Bull. Seismol. Soc. Am.*, *92*, 1281–1289, 2002.

Kilb, D., J. Gomberg, and P. Bodin, Triggering of earthquake aftershocks by dynamic stresses, *Nature*, *408*, 570–574, 2000.

Kirschvink, J. L., The least-squares line and plane and the analysis of palaeomagnetic data, *Geophys. J. R. Astron. Soc.*, *62*, 699–718, 1980.

Lin, G., Three-dimensional seismic velocity structure and precise earthquake relocations in the Salton Trough, southern California, *Bull. Seismol. Soc. Am.*, *103*, 2694–2708, 2013.

*Lin, G., Three-dimensional compressional attenuation model (Qp) for the Salton Trough, southern California, *Bull. Seismol. Soc. Am.*, *104*, 2579–2586, 2014.

*Lin, G., In situ V_p/V_s ratio variations in the Salton Sea Geothermal Field, southern California, *to be submitted*, 2016.

Lin, G., and P. G. Okubo, A large refined catalog of earthquake relocations and focal mechanisms for the Island of Hawai'i and its seismotectonic implications, *J. Geophys. Res.*, p. 2016JB013042, 2016.

Lin, G., and P. M. Shearer, Estimating local V_p/V_s ratios within similar earthquake clusters, *Bull. Seismol. Soc. Am.*, *97*, 379–388, 2007.

Lin, G., and P. M. Shearer, Evidence for water-filled cracks in earthquake source regions, *Geophys. Res. Lett.*, *36*, 2009.

*Lin, G., and Q. Zhang, Remote triggering inside versus outside geothermal fields in California, *SSA Meeting Abstracts*, 2016.

Matthews, M. V., and P. A. Reasenberg, Statistical methods for investigating quiescence and other temporal seismicity patterns, *Pure Appl. Geophys.*, *126*, 357–372, 1988.

Reasenberg, P. A., and R. W. Simpson, Response of regional seismicity to the static stress change produced by the Loma Prieta earthquake, *Science*, *255*, 1687–1690, 1992.

Shearer, P. M., G. A. Prieto, and E. Hauksson, Comprehensive analysis of earthquake source spectra in Southern California, *J. Geophys. Res.*, *111*, B06,303, doi:10.1029/2005JB003,979, 2006.

Thurber, C., and D. Eberhart-Phillips, Local earthquake tomography with flexible gridding, *Comput. Geosci.*, *25*, 809–818, 1999.

Thurber, C. H., Local earthquake tomography: velocities and V_p/V_s-theory, *in: Seismic Tomography: Theory and Practice*, pp. eds. H. M. Iyer and K. Hirahara, Chapman and Hall, London, 563–583, 1993.

Yang, W., E. Hauksson, and P. M. Shearer, Computing a large refined catalog of focal mechanisms for Southern California (1981–2010): temporal stability of the style of faulting, *Bull. Seismol. Soc. Am.*, *102*, 1179–1194, 2012.

*Zhang, Q., G. Lin, Z. Zhan, X. Chen, Y. Qin, and S. Wdowinski, Absence of remote earthquake triggering inside geothermal production fields, *Geophys. Res. Lett.*, *submitted*, 2016.